Lago Loreley, Selene (Orcid ID: 0000-0003-2980-8110)
Saraceno Martin (Orcid ID: 0000-0002-5657-4420)
Piola Alberto, R. (Orcid ID: 0000-0002-5003-8926)
Paniagua Guillermina, F. (Orcid ID: 0000-0002-7460-3897)
Ferrari Ramiro (Orcid ID: 0000-0001-5220-4580)
Artana Camila, Indira (Orcid ID: 0000-0002-0968-8580)
Provost Christine (Orcid ID: 0000-0003-4693-3685)

On the wind contribution to the variability of ocean currents over wide continental shelves: a case study on the northern Argentine continental shelf

L. S. Lago[1,2,3], M. Saraceno[2,3,4,*], P. Martos[1,5], R. A. Guerrero[1,5], A. R. Piola[2,6], G. F. Paniagua[2,3,4], R. Ferrari[2,3,4], C. I. Artana[7], C. Provost[7]

[1] Instituto Nacional de Investigación y Desarrollo Pesquero, Mar del Plata, Argentina

[2] Departamento de Ciencias de la Atmósfera y de los Océanos, FCEN, Universidad de Buenos Aires, Buenos Aires, Argentina

[3] Unidad Mixta Internacional-Instituto Franco-Argentino para el Estudio del Clima y sus Impactos (UMI-IFAECI/CNRS-CONICET-UBA), Buenos Aires, Argentina

[4] Centro de Investigaciones del Mar y la Atmósfera (CIMA-CONICET/UBA), Buenos Aires, Argentina

[5] FCEyN, Universidad Nacional de Mar del Plata, Buenos Aires, Argentina.

[6] Departamento de Oceanografía, Servicio de Hidrografía Naval (SHN), Buenos Aires, Argentina

[7] Laboratoire LOCEAN-IPSL, Sorbonne Université (UPMC, Univ. Paris 6) -CNRS-IRD-MNHN Paris, France

* Corresponding author: Loreley Selene Lago (loreley.lago@cima.fcen.uba.ar)

Key Points:

• 11 months of in-situ velocities at two sites of the Argentine continental shelf are analyzed.

• The barotropic component explains 83% of the total variance and the along-shore velocities at the two sites are highly correlated (0.86).

• Along-shore wind stress causes across-shore pressure gradients that modify the along-shore currents.

Abstract

The Southwestern Atlantic Ocean has one of the largest and most productive continental shelves of the southern hemisphere. Despite its relevance, its circulation patterns have been largely inferred from hydrographic observations and numerical models. Here we describe the variability of the shelf circulation based on the analysis of eleven months of multi-level currents measured by two bottom-mounted acoustic Doppler current profilers deployed over the continental shelf at 39°S. The record-length mean is 12 cm s^{-1} and 13 cm s^{-1} in the upper layer and decreases to 6 cm s^{-1} and 8 cm s^{-1} near the bottom, at the deployment nearer and further from the coast respectively. The mean flow direction is towards the NE, following the orientation of the isobaths. Measurements at both sites show that the along-shore barotropic component accounts for 83% of the variability observed and are well correlated (0.86), suggesting a relatively uniform flow, which is presumably driven by large-scale forcing. Indeed, large scale wind stress patterns dominate the temporal variability of the in-situ currents and the passage of atmospheric fronts induces significant changes in the observed currents at all depths. We found that for 12 % of the measurements the currents reverse the direction to the SW in response to these atmospheric patterns. Furthermore, the analysis of sea surface height reconstructed from bottom pressure measurements at both sites and from a coastal tide gauge reveals that the variability of the along-shore currents is driven by the cross-shore pressure gradients generated by the along-shore wind stress.

1 Keywords

• OCEAN CIRCULATION

• IN-SITU TIME SERIES

• WIND

• LOW-FREQUENCY VARIABILITY

• ARGENTINE CONTINENTAL SHELF

• SOUTHWESTERN ATLANTIC

1 Introduction

The Argentine continental shelf (ACS) is the largest of the southern hemisphere and one of the most productive ecosystems of the world ocean (Bisbal, 1995; Acha et al., 2004). Off the shelf and north of about 38°S, the circulation is characterized by the poleward flow of the warm and saline Brazil Current (BC). South of 38°S, the equatorward Malvinas Current (MC) carries cold and relatively fresh waters along the shelf-break (Gordon, 1989; Figure 1a). Both currents collide near 38ºS generating a highly energetic region known as the Brazil/Malvinas Confluence, which is characterized by the formation of warm and cold core eddies and filaments (Garzoli & Garraffo, 1989). Numerical simulations indicate that variations in the intensity of the MC and the BC lead to changes in the cross-shore pressure gradient over the shelf and slope and therefore modulate the strength of the along-shore flow over the shelf (Palma et al., 2008; Matano et al., 2010).

Our understanding of the dynamics governing the circulation over the shelf is limited due to the scarce number of direct observations of currents. Consequently, several studies inferred circulation patterns from property distributions (Piola et al., 2000; Lucas et al., 2005; Piola et al., 2008a, 2008b; Möller et al., 2008). These studies concluded that the circulation between 43ºS and 38ºS is mainly to the NE (Figure 1a) and that currents are more intense in autumn and winter and less intense in spring and summer. To the best of our knowledge,

reversal of the circulation was not reported in this region based on in-situ velocity measurements, but it was previously suggested for the spring and summer seasons in the coastal region near the Plata River by the analysis of temperature and salinity distributions (ie Lucas et al., 2005). Numerical simulations suggest that the inner and middle shelf circulation is primarily driven by the along-shore component of the wind stress (Palma et al., 2004). Seasonal geostrophic currents derived from satellite altimetry data south of 36°S present a mean flow to the north all year-round, with weak seasonal variability, and a slight wind-driven increase in autumn-winter (April–July) (Strub et al., 2015; Ruiz-Etcheverry et al., 2016). Short-term observations (Lanfredi & Capurro, 1971; Lanfredi, 1972) along with numerical models (Forbes & Garrafo, 1988; Combes & Matano, 2018; Glorioso & Flather, 1995), also show a mean flow in the ACS towards the NNE and indicate that tidal currents north of 40°S are relatively weak. Rivas (1997) analyzed an array of three current-meter moorings off Peninsula Valdes (43°S, Figure 1a) and found that the spectral energy of low-frequency variability (periods longer than 1.5 days) increases with the distance from the coast. Rivas (1997) also found that periodicities between 2 and 10 days are linked to the passage of atmospheric cyclones coming from the west. Variability at periods longer than 10 days might be related to the interaction of the MC with the shoaling shelf bathymetry (Glorioso & Flather, 1995).

The shelf area considered in this study is the portion of the ACS located off Mar del Plata (Argentina) between 37°S and 40°S and 56°W and 59°W (Figure 1). At this location, the continental shelf is shallower than 200 m and isobaths have a predominant SW – NE orientation. Our main objective is to describe the shelf circulation in this region based on the analysis of direct observations of currents collected at two sites located in the inner and mid-shelf regions around 39°S, and to identify the main forcing mechanisms that drive the low-frequency variability (Figure 1b). In the following, we refer to low-frequency variability as the variability of periods longer than 48 h. The article is organized as follows: data are described in section 2, the methodology applied in section 3, and results and discussion are presented in sections 4 and 5 respectively.

2 Data

2.1 In-situ data

The data analyzed in this study were collected as part of French-Argentinian CASSIS project (www.cima.fcen.uba.ar/malvinascurrent), which was designed to further understand the ocean dynamics of the Southwestern Atlantic Ocean (SAO), with a focus on the MC, the circulation in the ACS, and their interaction. To achieve this purpose, an array of moorings equipped with current-meters, conductivity, temperature and pressure recorders was deployed at selected locations over the SAO. This paper describes the observations obtained over the continental shelf (Saraceno et al., 2019), collected by two upward-looking 300 kHz Acoustic Doppler Current Profilers (ADCPs) deployed under track #26 of the Jason-2 (J2) satellite mission. The onshore site was located at 68 m depth at around 60 km from shore and the offshore site at 90 m depth at 154 km from shore (Figure 1b). Hereafter, these sites are referred to as A1 and A2, respectively. The ADCP configuration consisted on a 20° beam angle, a bin width of 4 m and an average time-interval of 15 minutes. For this set of parameters, the nominal accuracy of the horizontal velocity was 3.6 cm s^{-1}. Each ADCP was housed in a bottom cage developed by IFREMER (http://wwz.ifremer.fr/), along with conductivity (C), temperature (T) and pressure (P) Sea-Bird SBE 37-IM MicroCAT, installed 0.6 m above the sea floor. The SBE37 MicroCAT were set to measure with a sample interval of 1 h, each measurement consists on the average of ten samples recorded with a time

difference of 2.4 seconds, and the associated resolution of the pressure sensor is 0.84 mm. Before the deployment, once the ADCPs and the other sensors were mounted on the corresponding cages, we carried out the compass calibration following the WorkHorse Monitor ADCP User's Guide (R. D. Instruments, 2001). We repeated the calibration until the overall error was less than 5°. All instruments recorded data hourly. The ADCPs were set to sample the current profiles with a vertical resolution of 4 m, thus there are 16 vertical bins at A1 and 21 bins at A2. The deployment (18 December 2014) and recovery (21 November 2015) was done with the offshore rescue vessel SB-15 Tango of Prefectura Naval Argentina. A close inspection of the velocity time series at the two shallowest levels shows that, despite having similar variability to the levels below, their amplitude and direction is random (not shown). This can be associated with the presence of bubbles in the shallowest levels (Zedel, 2001). Therefore, we considered ADCP data at A1 and A2 with no gaps at 14 and 19 levels, from 62 m to 10 m depth and from 84 m to 12 m depth, respectively. To the best of our knowledge, the time series obtained are the longest recorded so far in the northern ACS.

We also employed historical hydrographic data obtained from conductivity-temperature-depth (CTD) profilers collected in the study area from June 1986 through March 2014, kindly provided by Instituto Nacional de Investigación y Desarrollo Pesquero (INIDEP, Argentina) and sea surface height (SSH) data from a coastal tide gauge (TG) located in Mar del Plata at 38.0ºS 57.5ºW (Figure 1b) available at https://uhslc.soest.hawaii.edu/.

The rest of the physical data collected are used to help the understanding of these time series. A detailed analysis of the 11-months bottom T and S measurements, along with a description of the water masses of this area of study, is the subject of a complementary work.

2.2 Satellite data

Sea Surface Temperature (SST) was extracted from the Multi-Scale Ultra-High Resolution (MUR) data base (https://mur.jpl.nasa.gov/). MUR consists of a multi-mission L4 daily mean product with a spatial resolution of 1 km. It combines different satellite SST data (infrared radiometers like Moderate Resolution Imaging Spectroradiometer (MODIS) and Advanced Very High Resolution Radiometer (AVHRR), microwaves radiometers like Advanced Microwave Scanning Radiometer for Earth Observing System (AMSR-E), Advanced Microwave Scanning Radiometer 2 (AMSR2) and WindSat, and also in-situ data from buoys.

2.3 Reanalysis

We use the ERA-Interim reanalysis data produced by the European Center of Middle-range Weather Forecast (ECMWF) (Berrisford et al., 2009) which consists of 40 years of global analysis of atmospheric fields based on an assimilation system of global data included in a numerical model. In this study, we used the 6-hourly wind stress and Sea Level Pressure (SLP) data available globally with a 0.75° spatial resolution from the ERA-Interim database (https://www.ecmwf.int/en/forecasts/datasets/archive-datasets/reanalysis-datasets/era-interim).

We also considered NCEP (Kalnay et al., 1996) and CCMP (Atlas et al., 2009) winds. The ERA-Interim wind stress data were selected because it led to smaller differences with in-situ measurements obtained by a meteorological buoy deployed at the shelf-break during the CASSIS project (Table A1).

3 Methodology

The main isobath orientation at each deployment is 68° at A1 and 53° at A2, measured clockwise from True North. These orientations were used to decompose the currents at each site into along-bathymetry and across-bathymetry components. Because the bottom slope at A1 is much steeper than at A2 (Figure 1b) the determination of the isobath orientation at the latter is subtler than at A1. For this purpose, we used the data from the General Bathymetric Chart of the Ocean (GEBCO, 2003) combined with the bathymetry measurements from Servicio de Hidrografia Naval (SHN), mostly in the inner-shelf. Although the GEBCO bathymetry presents inconsistencies of several meters with the local depth near A2, these discrepancies do not lead to significant changes in the isobath orientation. The angle selected to decompose the direction of the currents at A2 considers the mean direction of the isobaths in a circle of 70 km radius around the position of this deployment. The 53° orientation estimated at A2 coincides with the direction of the time-average de-tided velocity recorded at the deepest level (Table 1), suggesting that bottom topography from GEBCO agrees reasonably well with that of the real ocean.

To analyze the main frequencies present in the velocity observations, we computed the spectrum of the unfiltered along-bathymetry current in the shallowest level of each mooring (Figure 2). It shows that the predominant variability is found at the diurnal, semi-diurnal (both associated with tides) and also at the inertial frequencies (18.7 h at the latitude of the deployments). As we focused the analysis on the low-frequency variability, the hourly time series were de-trended and low-pass filtered with a cut-off period of 48 h to remove inertial and tidal variability. The filter applied reduced the total variance by 40% (55%) at A1 (A2) for the along-bathymetry component and by 71% (81%) at A1 (A2) for the across-bathymetry component.

Vector correlation (VC) between the observed currents and the local wind stress was computed following Kundu (1976). This method provides a complex number whose magnitude (< 1) gives the overall measure of correlation and whose phase angle (α) gives the average counterclockwise angle of the second vector relative to the first one. We computed the vector correlation using the wind stress as the first vector and the current as the second vector. Thus, a positive phase results if the average direction of the currents is α degrees counterclockwise relative to the mean wind direction; in other words, if the current is, on average, α degrees to the left of the wind. It is important to note that this method does not indicate the geographical direction of the vectors and only refers to the mean angle difference between both vectors analyzed.

We also estimated the Ekman depth as the depth at which Ekman currents have decreased their magnitude in e^{-1} relative to the velocity at a 10 m depth, considering turbulent viscosity coefficient values that range between 100E-4 and 500E-4 m^2 s^{-1} (Elipot et al., 2009). The estimated Ekman depths considering ERA-Interim winds range between 14 m and 34 m at A1 and between 16 m and 32 m at A2.

To further analyze the nature of the velocity observations, we de-composed the velocity vectors into a barotropic and a baroclinic component. At each time step, the barotropic component was estimated as the vertical average of the velocities observed at all depth levels. The baroclinic component was estimated by subtracting the barotropic one from the total velocity at each level. Then, to quantify how large the baroclinic component of the observed currents is, we estimated a baroclinicity index as the sum of the absolute value of the vertical shear every 4 m in the vertical.

Using bottom pressure measurements at A1 and A2, and SSH data from TG, we estimated the cross-section relative geostrophic velocity (Eq.1). We considered the sea surface as the reference level.

$$V_{g\,relative} = \frac{g}{f}\frac{\partial SSHa}{\partial x} \quad (1)$$

Where SSHa is the SSH anomaly, x represents the along-section axis. As the cross-section direction coincides with the along-shore orientation, hereinafter we refer to the cross-section component as the along-shore component, and to the along-section component as the cross-shore component.

We estimated the $V_{g\,relative}$ between the TG and A1 (Vg_a), and also between A1 and A2 (Vg_b, see Figure 1b for location). To compute the SSHa we used the bottom pressure observations at A1 and A2 (Eq. 2):

$$SSH = \frac{1}{\rho g}(P - P_{atm}) \quad (2)$$

Where P_{atm} represents the atmospheric SLP from ERA-Interim reanalysis, g is the acceleration of gravity (9.8 m s^{-2}) and ρ the water density. Density (ρ) was estimated following the International Thermodynamic Equation of Seawater (IOC, SCOR, & IAPSO, 2010). Because in-situ vertical profiles of T and S during the period of observation are not available, to estimate the contribution of the density variations with depth, we used a seasonally varying vertical profile estimated from the historical hydrographic data. A significant seasonal thermocline establishes each year in this region (Carreto et al., 1995; Lucas et al., 2005; Auad & Martos, 2012). To account for the corresponding changes in the density field, we repeated the vertical density estimate for each season and re-estimated the SSH with the four seasonal density profiles computed with the historical values described in Section 2.1. The largest difference between the seasonal estimates of SSH was found between the winter and summer months (4 cm at A1 and 3 cm at A2).

The above-described calculations only provide estimates of the time variability of the geostrophic currents. To estimate absolute geostrophic velocities, we assumed that the time-averaged barotropic velocities observed at A1 and A2 are in geostrophic balance and we inferred the mean SSH gradients required to achieve geostrophic balance. Therefore, for the calculus of the absolute geostrophic velocity we added the mean SSH gradient to the SSHa at each time step. For the inner shelf region between TG and A1 (Vg_a) we used the time-average barotropic velocity at A1, while for the mid-shelf region between A1 and A2 we used the time-average of the barotropic velocities observed at A1 and A2. We considered the cross-section (along-shore) velocities, i.e. the component of velocities orthogonal to the section that passes over the TG, A1 and A2 (Figure 1a and 1b). This section is 152° clockwise from True North and is aligned with the cross-shore direction. The barotropic component in this case was estimated as the vertical average of the velocities excluding the Ekman layer.

4 Results

4.1 Mean flow and variability: bathymetric control

The record-length mean speed and direction, and the maximum velocities at all depths of in-situ measurements obtained at A1 and A2 (Figure 1) are listed in Table 1. The record-length mean speed at both sites decreases with depth (Table 1). The mean speed at the shallowest level reaches 12 cm s^{-1} at A1 and 13.1 cm s^{-1} at A2. At both sites, the upper layer rotates first anti-clockwise (up to 26 m for A1 and 34 m for A2), then clockwise down to the

bottom. These results are consistent with the surface to bottom Ekman dynamics spiral reversal due to wind and bottom frictional effects.

Figure 3 shows the variance ellipses at all depths at A1 and A2, and the mean vector of the shallowest and deepest levels considered. At both sites, the major axis of the variance ellipses of the observed currents display a clockwise rotation with depth and no change in magnitude. The mean vector of the deepest level is aligned with the local bathymetry. At A1, the variance ellipses are more elongated than at A2, i.e. the axis in the across-bathymetry (along-bathymetry) direction is smaller (larger) at A1 than at A2, and on average the principal axis is 6 times larger than the secondary axis at A1, while at A2 is only 2 times larger. This difference could be due to the fact that the bottom slope is steeper at A1 (Figure 1b) than at A2, suggesting that the flow is more effectively steered by the bottom topography at A1.

In-situ velocity time series of the along-bathymetry ($vel_{//}$) and cross-bathymetry (**$vel_\perp$**) components for selected depths at A1 and A2 are shown in Figures 4 and 5, respectively. The corresponding Hovmöller diagrams, considering all available levels, can be found in Figures A1 and A2. At both sites, the magnitude of the currents is, in general, higher at shallower depths. The along-bathymetry component is larger than the cross-bathymetry component at all levels, particularly in the deepest ones. The along-bathymetry component has a very homogeneous vertical profile, suggesting that the barotropic component dominates the circulation.

4.2 Dominance of the barotropic circulation

We estimated the barotropic component of the unfiltered in-situ velocities in the along-shore direction as explained in Section 3. The resulting time series at A1 and A2 (Figure 6a) show similar variability. In fact, the correlation coefficient between them is 0.86, significant at a 95% confidence level (CL). Moreover, they are highly coherent (Figure 6b), with values near 1 for tidal periods (12 h and 1 day), above 0.8 for periods longer than 1 day, and near 0.7 for the 6 h period. They are also coherent for the inertial period (0.77) although it is not visible in Figure 6b due to the window-size used to compute the coherence (24 h). If the window-size is reduced (ie 7 h), the inertial peak is distinct from the diurnal tidal peak (not shown). All these results strongly indicate that the along-shore barotropic flow is relatively uniform in this portion of the ACS. The cross-shore component at A1 and A2 presents significant but low correlation (0.4) and their coherence is high only at tidal frequencies, with values near 1 for the semi-diurnal component of the tidal signal (not shown).

We also investigated the connection between the circulation in the continental shelf and the circulation near the shelf break by comparing velocity observations from A2 and a mooring deployed at 1000 m depth located at 40.2°S and 55.9°W (A4, see Figure 1a), which is under the influence of the strong MC. A full description of the velocities at A4 and their variability can be found in Paniagua et al. (2018), and in-situ data from A4 are available at Saraceno et al. (2017). The comparison between the unfiltered along-bathymetry currents at A2 and A4 does not reveal a clear influence of the MC variability over the continental shelf circulation: all correlation coefficients computed between different depth levels of both deployments are not significant, and only shows a significant but low coherence value at semi-diurnal tidal frequency (not shown). We repeated the comparison with the 20-day low-pass filtered along-bathymetry component of the barotropic velocities at A2 and A4, and in this case no significant correlation was found either. A4 reveals a period of relative low

velocities from approximately May 2015 to September 2015 (Paniagua et al., 2018), while at A2 there is no clear change in the intensity of the currents for that period.

To further study the variability of the observed velocities, we carried out an EOF analysis to analyze the variability of the zonal and meridional velocity components of the two moorings at all depth levels as the input. Thus, the spatial patterns display the horizontal velocity vectors and are visualized in the cross-shore vertical section that contains both moorings (Figure 7). The two leading modes depict the dominant spatio-temporal variability of the ensemble of the measurements obtained at the two moorings: together, they account for 89 % of the total variance. The first EOF mode (Figures 7a and 7c) explains 82.8% of the variance and depicts, at both sites, a circulation to the NE nearly homogeneous in the vertical. In fact, this mode is in good agreement (correlation coefficient 0.95) with the along-shore component of the barotropic velocity of A1 and A2. This result confirms that the barotropic mode dominates the low-frequency circulation in the region. We computed the SLP composite for the days of minimum values of the first EOF time series (Figure A3a) and for the days of maximum values of the first EOF time series (Figure A3b). The pattern of the first EOF mode (northeastward barotropic velocity profile) is associated with a low-pressure system that induces a circulation to the NE in the location of the deployments, and vice versa. The second mode (Figures 7b and 7d) explains only 6.3% of the variance. The vertical structure of the second mode at A1 shows that below 50 m depth the currents are oriented towards the east, while above 50 m the direction is towards the NE, similar to the direction of the first mode. At A2, the vertical structure of the second mode is distinct from the first one, as currents rotate from the SE at the surface to the S up to 60 m depth and to the N below that depth. Despite the much lower variance explained by the second mode, the occurrence of this mode might have important consequences in the ecosystem around A2: a clockwise rotation of the velocity vectors with increasing depth could be associated with downwelling, which could limit the nutrient flux to the photic layer.

4.3 Baroclinicity and stratification

In this section we aim to study the baroclinic behavior of in-situ velocities, in particular, exploring possible changes in the vertical structure of the currents associated with the vertical stratification. To achieve this goal, we compare the difference between the sea surface temperature (MUR SST) and the bottom (in-situ measurements) with the baroclinicity index defined in Section 3 at A1 (Figure 8) and at A2 (Figure 9).

At A1 the water column is thermally stratified until May 2015, from May to late October 2015 the vertical stratification weakens considerably (Figure 8a). In contrast, although at A2 the SST shows a seasonal cycle similar to the one observed at A1, the bottom T, which is colder and less variable than at A1, is always lower than the SST throughout the observation period (Figure 9a). The difference between surface and bottom T at A2 is lowest (2 ℃) from late June to late October 2015. These observations indicate that although the vertical stratification at A2 is seasonally modulated, it is maintained during winter. The analysis of the baroclinicity index (Figures 8b and 9b) indicates that, at both sites, an increased vertical stratification of the water column is associated with a more baroclinic flow. During the period of strong stratification (from January to April 2015), the mean value of the baroclinicity index was 0.05 s^{-1} at A1 and 0.04 s^{-1} at A2; these values decreased in the period of no-stratification at A1 and of weak-stratification at A2 (from July to October 2015) to 0.02 s^{-1} and 0.03 s^{-1}, respectively. Hence, the effect of stratification in relation to the baroclinicity of the flow resulted more evident at A1, when the water column is homogeneous the baroclinicity index was reduced 60% with respect to the stratified period.

The largest peaks in the baroclinic index time series are often associated with drops in the bottom T (Figure 8 and 9), indicating that some of these events are associated with cooling of bottom waters. But bottom cooling events might be likely due to lateral (cross-shore) advection (Figure A4). Indeed, the comparison of the bottom T at A1 with the cross-shore velocity near the bottom (at 58 m depth) shows that the majority of the bottom cooling events are preceded by an intense onshore velocity (positive cross-shore velocity), suggesting onshore advection of relatively cold waters.

Based on Figures 8a and 9a we defined two periods: a stratified period from 1 January 2015 to 31 March 2015 and a well-mixed period from 1 July 2015 to 30 September 2015 in order to further analyze the effect of stratification on the circulation. In Figure 10 we present the time-average and standard deviation of the along-shore velocity at each level, during the stratified and the well-mixed periods. We observe that the time-averaged velocities and standard deviations of both sites are larger during the well-mixed period, that coincides with stronger winds (see also Figure A5). During winter the heat-flux is negative, hence wind-mixing might affect the vertical velocity profile without changing significantly the temperature gradient. Wind enhances vertical mixing in the upper layer and also modifies significantly the velocity magnitudes, as will be discussed in Section 4.5.

4.4 Geostrophic adjustment and wind forcing

We computed the geostrophic velocity from SSHa data following eq. 1 (see Section 3), between the TG located at Mar del Plata and A1 (Vg_a) and between A1 and A2 (Vg_b). Hereinafter we present the analysis of the 48 h low-pass filtered data in order to study the low-frequency variability of the in-situ currents.

Geostrophic velocities obtained from SSHa and direct observations are highly correlated (Figure 11). The comparison between Vg_a and the barotropic velocity at A1 resulted in a correlation coefficient of 0.86, and between Vg_b and the average of the barotropic velocity at A1 and A2 of 0.96 (95% CL). These results strongly suggest that the barotropic velocity component is in near-geostrophic balance and that the circulation in the along-shore direction is very uniform, as suggested in the previous section.

During the period of observations, the mean local wind speed was 7 m s^{-1} and the mean direction was from the WNW. The most intense winds were recorded in winter (Figures 4a, 5a and A5). There is a noticeable coherence between the wind stress and the time series of the currents, at all depths (Figures 4 and 5). To further quantify this observation, we computed the VC (cf Section 3) between wind stress time series from the ERA-Interim reanalysis and the in-situ currents at different depths (Figure A6). VC values range between 0.56 and 0.59 at A1 and between 0.46 and 0.57 at A2, all significant at a 95% CL. These results suggest that, at both sites, wind stress affects the currents throughout the water column.

The correlation between along-shore in-situ currents and the along-shore wind stress is 0.7 at 95%CL (Figure 12). The largest correlation is obtained at lag 0, suggesting that the variability of the along-shore geostrophic velocities is modulated by the cross-shore pressure gradient generated by the along-shore wind stress through Ekman dynamics, and that the response of the along-shore currents to the along-shore wind stress is produced in less than 48 h. Positive wind stress (towards the NE) piles-up water near the coast, creating a barotropic cross-shore pressure gradient which increases the along-shore geostrophic velocities (towards

the NE). This means that there is a geostrophic influence of the local wind stress over the circulation of the region.

<u>4.5 Fast flow reversal events</u>

The in-situ velocity data analyzed revealed several events where currents abruptly changed direction and eventually reversed in less than 5 days (Figures 4 and 5). Hereinafter we refer to those events as current reversals. The relatively strong reversal event observed from 28 April 2015 to 4 May 2015 is characterized by a change of direction of in-situ currents from NE to SW and back to NE. Comparison of the SLP distribution on 28 April 2015 and the climatological distribution in the fall (Figure 13), reveals that an anomalous high-pressure system centered south of the location of the deployments induced a counterclockwise circulation pattern and easterly winds over the mooring sites. The SLP pattern observed is consistent with a decrease in the magnitude of northeastward currents, or even the inversion of these currents to the south. This result further confirms the strong coupling between the local winds and the shelf circulation throughout the water column. This event was particularly clear in the along-shore velocity at the shallowest level available at A1, therefore we searched for other reversal events in the along-shore velocity at this level. We identified 40 reversal events (12 % of the record) using the following criteria: in-situ currents at the shallowest level of A1 were southwestward and exceeded -5 cm s^{-1} (lower than the mean value minus one standard deviation). There were between 1 and 3 reversal events each month that lasted between 3 and 14 days. This is in agreement with the frequency of passage of cold and warm atmospheric fronts over the region (Garreaud, 2000; Solman & Orlanski, 2014; Ribeiro et al., 2016). The composite of SLP for those days (Figure A7) shows that these reversal events coincide with the presence of a high-pressure system located SE of the mooring sites that induces an along-shore wind stress component to the W over the location of the deployments, and to the SW northeast of the deployments. As previously observed (section 4.4), this wind stress pattern is consistent with a geostrophic velocity response of the currents that can be reversed to the SW.

5 Summary of results and discussion

The longest available velocity time series recorded at two sites near 39ºS in the Argentine Continental Shelf were analyzed in this study. In-situ currents show a mean NE direction, consistent with the circulation inferred from property distributions (Lucas et al., 2005; Piola et al., 2008a, 2008b, 2000; Möller et al., 2008), satellite altimetry (Ruiz-Etcheverry et al., 2015; Strub et al., 2015) and numerical model outputs (e.g. Glorioso & Flather, 1995; Palma et al., 2008, Combes & Matano, 2018). The velocity magnitude of the in-situ measurements is maximum in the shallowest level and decreases with depth, at both sites. Velocities are larger in the deployment closer to shore: at A1 maximum velocity is 61.3 cm s^{-1} at 10 m depth while at A2 the maximum observed velocity was 47.4 cm s^{-1} at 12 m depth. The alignment of the time-average currents at the bottom with the local bathymetry suggests a topographic control of the flow over the continental shelf, consistent with previous observations carried out at ~43°S (Rivas, 1997). This alignment is stronger at A1, where the bottom slope is steeper. Direct velocity measurements at A1 and A2 are highly correlated. The first EOF mode of the in-situ velocities explains 83% of the total variance and represents the barotropic component of these velocities. As might be expected, at both sites the baroclinic component is larger during the stratified period (mostly from January to April 2015) than during the well-mixed period (from July to November 2015).

In this study, we show that the influence of the wind extends throughout the water column. Indeed, the variability of the barotropic component of the velocities is closely

associated with the changes in the along-shore component of the wind stress (correlation coefficient = 0.7). This can be simply explained considering that the along-shore wind stress generates variations in the cross-shore barotropic pressure gradient that lead to the variations of the along-shore geostrophic velocities. The detailed analysis of the time series shows that sudden current reversals throughout the water column are observed in response to the passage of atmospheric fronts, that reverse the direction of the dominant wind, similar to earlier observations obtained in the mid-shelf region further south (Rivas, 1997). Since the study area is characterized by the frequent passage (1-3 events per month) of both low-pressure and high-pressure atmospheric systems coming from the west and southwest with a duration of 3 to 14 days (Garreaud, 2000; Solman & Orlanski, 2014; Ribeiro et al., 2016), current reversals are expected to be a recurrent phenomenon. The frequency of passing pressure systems is higher in winter, as the semi-permanent high-pressure system over the Southwestern Atlantic Ocean, centered at ~30°S, displaces equatorward, and hence the region becomes more affected by more intense cyclogenic activity (Martos & Piccolo, 1988). Frequent current reversals might have a significant impact on the local ecosystem. For example, numerical models (ie Auad & Martos, 2012) suggest that changes in the flow strength may alter the availability and distribution of nutrients, which in turn impacts significantly small pelagic species. The analysis presented here is in good agreement with previous descriptions of the circulation derived from hydrographic data and from numerical models (Lucas et al., 2005; Combes at al., 2018). In a follow-up paper we will compare the in-situ velocities with satellite altimetry data and estimate the volume transport over the continental shelf from both sets of observations.

Acknowledgements

References

Acha, E. M., Mianzan, H. W., Guerrero, R. A., Favero, M., & Bava, J. (2004). Marine fronts at the continental shelves of austral South America: Physical and ecological processes. *Journal of Marine systems*, *44*(1-2), 83-105. https://doi.org/10.1016/j.jmarsys.2003.09.005

Atlas, R., Hoffman, R. N., Ardizzone, J., Leidner, S. M., & Jusem, J. C. (2009). *Development of a new cross-calibrated, multi-platform (CCMP) ocean surface wind product*. Paper presented at AMS 13th Conference on Integrated Observing and Assimilation

Systems for Atmosphere, Oceans, and Land Surface (IOAS-AOLS), Phoenix, Arizona, USA.

Auad, G., & Martos, P. (2012). Climate variability of the northern Argentinean shelf circulation: Impact on Engraulis Anchoita. *The International Journal of Ocean and Climate Systems*, *3*(1), 17-43. https://doi.org/10.1260/1759-3131.3.1.17

Berrisford, P., Dee, D. P. K. F., Fielding, K., Fuentes, M., Kallberg, P., Kobayashi, S., et al. (2009). The ERA-interim archive. *ERA report series*, (1), 1-16, ECMWF: Reading, UK. Retrieved from www.ecmwf.int/publications

Bisbal, G. A. & Bengtson, D. A. (1995). Development of the digestive tract in larval summer flounder. *Journal of Fish Biology*, *47*(2), 277-291. https://doi.org/10.1111/j.1095-8649.1995.tb01895.x

Carreto, J., Lutz, V. A., Carignan, M. O., Colleoni, A. D. C., & De Marco, S. G. (1995). Hydrography and chlorophyll a in a transect from the coast to the shelf-break in the Argentinian Sea. *Continental Shelf Research*, 15(2-3), 315-336. https://doi.org/10.1016/0278-4343(94)E0001-3

Combes, V., & Matano, R. P. (2018). The Patagonian shelf circulation: Drivers and variability. *Progress in oceanography, 167*, 24-43. https://doi.org/10.1016/j.pocean.2018.07.003

Elipot, S., & Gille, S. T. (2009). Ekman layers in the Southern Ocean: spectral models and observations, vertical viscosity and boundary layer depth. *Ocean Science Discussions*, *6*(2), 115-139. https://doi.org/10.5194/os-5-115-2009

Forbes, M. C. & Garraffo, Z. D. (1988). A note on the mean seasonal transport on the Argentinian Shelf. *Journal of Geophysical Research: Oceans*, *93*(C3), 2311-2319. https://doi.org/10.1029/JC093iC03p02311

Garreaud, R. (2000). Cold air incursions over subtropical South America: Mean structure and dynamics. *Monthly Weather Review, 128*(7), 2544-2559. https://doi.org/10.1175/1520-0493(2000)128<2544:CAIOSS>2.0.CO;2

Garzoli, S. L. & Garraffo, Z. (1989). Transports, frontal motions and eddies at the Brazil-Malvinas Currents Confluence. *Deep Sea Research Part A. Oceanographic Research Papers*, *36*(5), 681-703. https://doi.org/10.1016/0198-0149(89)90145-3

Glorioso, P. D. & Flather, R. A. (1995). A barotropic model of the currents off SE South America. *Journal of Geophysical Research: Oceans*, *100*(C7), 13427-13440. https://doi.org/10.1029/95JC00942

Gordon, A. L. (1989). Brazil-Malvinas Confluence–1984. Deep Sea Research Part A. *Oceanographic Research Papers*, 36(3), 359-384. https://doi.org/10.1016/0198-0149(89)90042-3

GEBCO, C. (2003). General Bathymetric Chart of the Ocean. *British Oceanographic Data Center*. Monaco, International Hydrographic Organization.

Instruments, R. D. (2001). WorkHorse Monitor ADCP User's Guide, *RI Instruments,* San Diego, CA.

IOC, SCOR, & IAPSO. (2010). The international thermodynamic equation of seawater: calculation and use of thermodynamic properties. Intergovernmental Oceanographic Commission, *Manual and Guides, 56,* 1-196, UNESCO.

Kalnay, E., Kanamitsu, M., Kistler, R., Collins, W., Deaven, D., Gandin, L., et al. (1996). The NCEP/NCAR 40-year reanalysis project. *Bulletin of the American Meteorological Society,* 77(3), 437-471. https://doi.org/10.1175/1520-0477(1996)077<0437:TNYRP>2.0.CO;2

Kundu, P. K. (1976). Ekman veering observed near the ocean bottom. *Journal of Physical Oceanography*, 6(2), 238-242. https://doi.org/10.1175/1520-0485(1976)006<0238:EVONTO>2.0.CO;2

Lanfredi, N. W. (1972). Resultados de mediciones directas de corrientes en el Atlántico sudoccidental. *Armada Argentina, Servicio de Hidrografía Naval*. H. 650/2, Buenos Aires, 107.

Lanfredi, N. W. and Capurro, L. R. (1971). Resultados de mediciones directas de corrientes en el Atlantico Sudoccidental. *Armada Argentina, Servicio de Hidrografía Naval*. H. 650/1, Buenos Aires, 109.

Lucas, A. J., Guerrero, R. A., Mianzan, H. W., Acha, E. M., & Lasta, C. A. (2005). Coastal oceanographic regimes of the northern Argentine continental shelf (34–43 S). *Estuarine, Coastal and Shelf Science*, 65(3), 405-420. https://doi.org/10.1016/j.ecss.2005.06.015

Martos, P. & Piccolo, M. C. (1988). Hydrography of the Argentine continental shelf between 38° and 42°S. *Continental Shelf Research*, 8(9), 1043-1056. https://doi.org/10.1016/0278-4343(88)90038-6

Matano, R., Palma, E. D., & Piola, A. R. (2010). The influence of the Brazil and Malvinas Currents on the Southwestern Atlantic Shelf circulation. *Copernicus Publications, Ocean Science (os), 6,* 983-995. http://dx.doi.org/10.5194/os-6-983-2010

Möller Jr, O. O., Piola, A. R., Freitas, A. C., & Campos, E. J. (2008). The effects of river discharge and seasonal winds on the shelf off southeastern South America. *Continental Shelf Research*, 28(13), 1607-1624. https://doi.org/10.1016/j.csr.2008.03.012

Palma, E. D., Matano, R. P., & Piola, A. R. (2004). A numerical study of the Southwestern Atlantic Shelf circulation: Barotropic response to tidal and wind forcing. *Journal of Geophysical Research: Oceans*, 109(C8). https://doi.org/10.1029/2004JC002315

Palma, E. D., Matano, R. P., & Piola, A. R. (2008). A numerical study of the Southwestern Atlantic Shelf circulation: Stratified ocean response to local and offshore forcing. *Journal of Geophysical Research: Oceans*, 113(C11). https://doi.org/10.1029/2007JC004720

Paniagua, G. F., Saraceno, M., Piola, A. R., Guerrero, R., Provost, C., Ferrari, R.,et al. (2018). Malvinas Current at 40° S–41° S: First Assessment of Temperature and Salinity Temporal Variability. *Journal of Geophysical Research: Oceans, 123*(8), 5323-5340. https://doi.org/10.1029/2017JC013666

Piola, A. R., Campos, E. J., Möller, O. O., Charo, M., & Martinez, C. (2000). Subtropical shelf front off eastern South America. *Journal of Geophysical Research: Oceans*, 105(C3), 6565-6578. https://doi.org/10.1029/1999JC000300

Piola, A. R., Möller Jr, O. O., Guerrero, R. A., & Campos, E. J. (2008a). Variability of the subtropical shelf front off eastern South America: Winter 2003 and summer 2004. *Continental Shelf Research*, 28(13), 1639-1648. https://doi.org/10.1016/j.csr.2008.03.013

Piola, A. R., Romero, S. I., & Zajaczkovski, U. (2008b). Space–time variability of the Plata plume inferred from ocean color. *Continental Shelf Research*, *28*(13), 1556-1567. https://doi.org/10.1016/j.csr.2007.02.013

Ribeiro, B. Z., Seluchi, M. E., & Chou, S. C. (2016). Synoptic climatology of warm fronts in Southeastern South America. *International Journal of Climatology*, *36*(2), 644-655. https://doi.org/10.1002/joc.4373

Rivas, A. L. (1997). Current-meter observations in the Argentine Continental Shelf. *Continental Shelf Research*, *17*(4), 391-406. https://doi.org/10.1016/S0278-4343(96)00039-8

Ruiz-Etcheverry, L. A., Saraceno, M., Piola, A. R., & Strub, P. T. (2016). Sea level anomaly on the Patagonian continental shelf: Trends, annual patterns and geostrophic flows. *Journal of Geophysical Research: Oceans*, *121*(4), 2733-2754. https://doi.org/10.1002/2015JC011265

Ruiz-Etcheverry, L. R., Saraceno, M., Piola, A. R., Valladeau, G., & Möller, O. O. (2015). A comparison of the annual cycle of sea level in coastal areas from gridded satellite altimetry and tide gauges. *Continental Shelf Research, 92*, 87-97. https://doi.org/10.1016/j.csr.2014.10.006

Saraceno, M., Guerrero, R., Piola, A. R., Provost, C., Perault, F., Ferrari, R., et al. (2017). Malvinas Current 2014–2015: Mooring velocities. SEANOE. https://doi.org/10.17882/51492

Saraceno M., Guerrero, R., Piola, A. R., Provost, C., Perault, F., Ferrari, R., et al. (2019). Argentine continental shelf currents 2014-2015: velocities, pressure and temperature. SEANOE. https://doi.org/10.17882/61777

Solman, S. A., & Orlanski, I. (2014). Poleward shift and change of frontal activity in the Southern Hemisphere over the last 40 years. *Journal of the Atmospheric Sciences*, 71(2), 539-552. https://doi.org/10.1175/JAS-D-13-0105.1

Strub, P. T., James, C., Combes, V., Matano, R. P., Piola, A. R., Palma, E. D., et al. (2015). Altimeter-derived seasonal circulation on the southwest Atlantic shelf: 27°–43° S. *Journal of Geophysical Research: Oceans*, *120*(5), 3391-3418. https://doi.org/10.1002/2015JC010769

Zedel, L. (2001). Using ADCP background sound levels to estimate wind speed. *Journal of Atmospheric and Oceanic Technology*, *18*(11), 1867-1881. https://doi.org/10.1175/1520-0426(2001)018<1867:UABSLT>2.0.CO;2
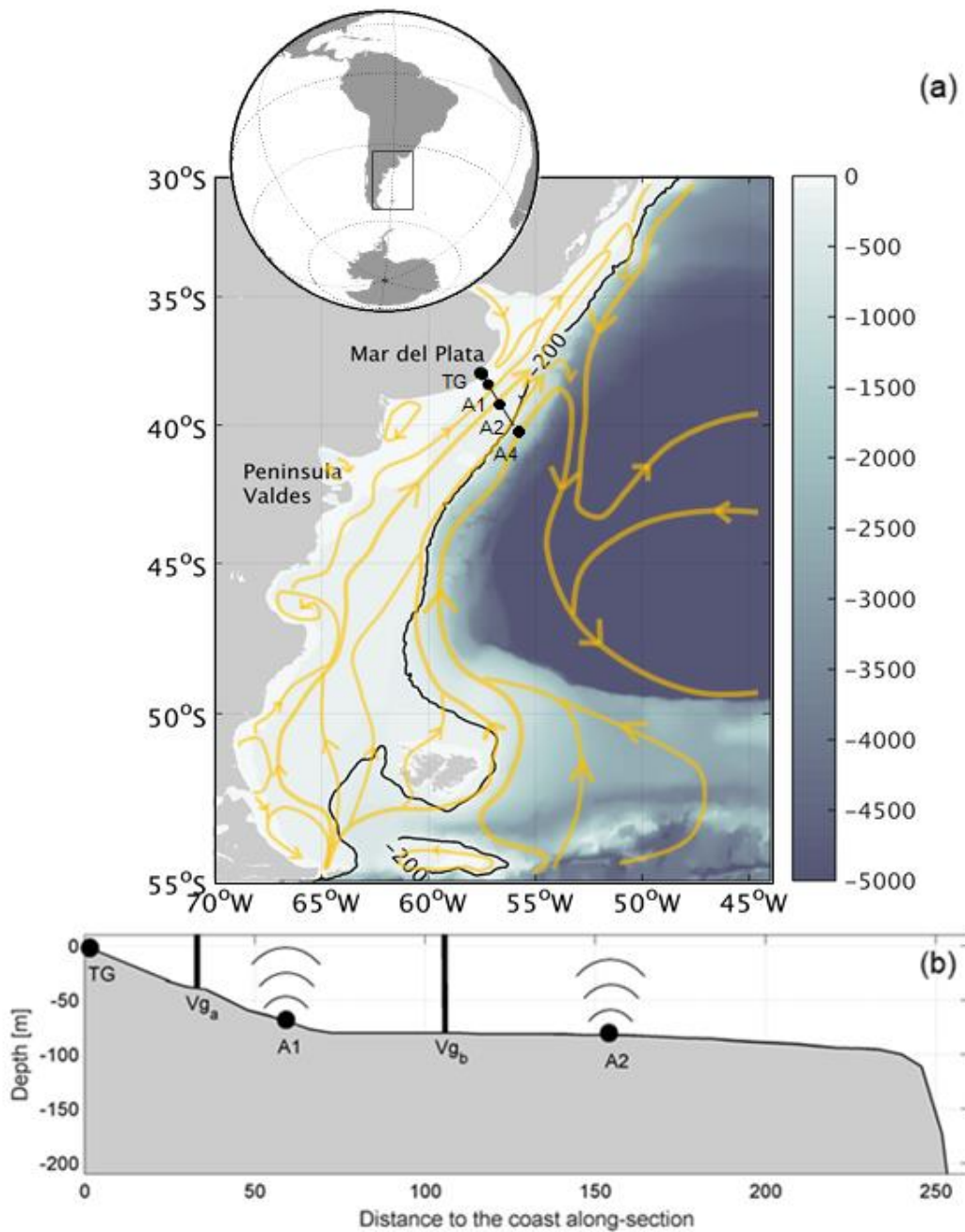
Figure 1: (a) Schematic surface circulation in the Southwestern Atlantic Ocean adapted from Matano et al. (2010). The 200 m isobath is indicated by the black line. Black dots show the location of the TG at Mar del Plata and of the deployments (A1 and A2). The black line near Mar del Plata depicts the section that passes over the mooring sites analyzed in this study. (b) Along-section bathymetry (GEBCO, 2003) (see thick black line in a). Black dots indicate the location of the Tide Gauge (TG) and moorings A1 and A2; vertical lines correspond to the position where geostrophic velocities have been computed from SSH data, between the TG and A1 (Vg_a) and between A1 and A2 (Vg_b).
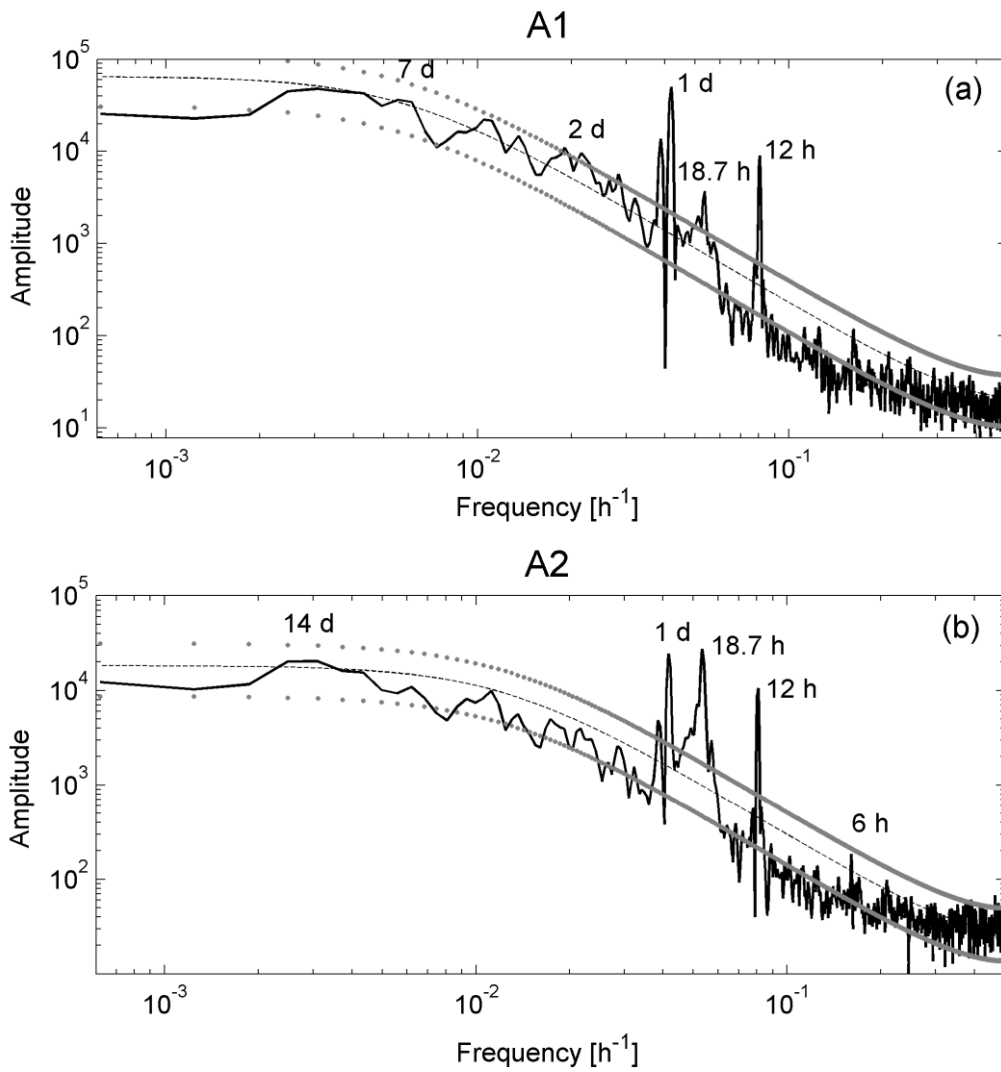
Figure 2: Along-bathymetry current spectra from the shallowest level, 10 m at A1 (a) and 12 m at A2 (b). The dotted lines indicate the 95% confidence level.
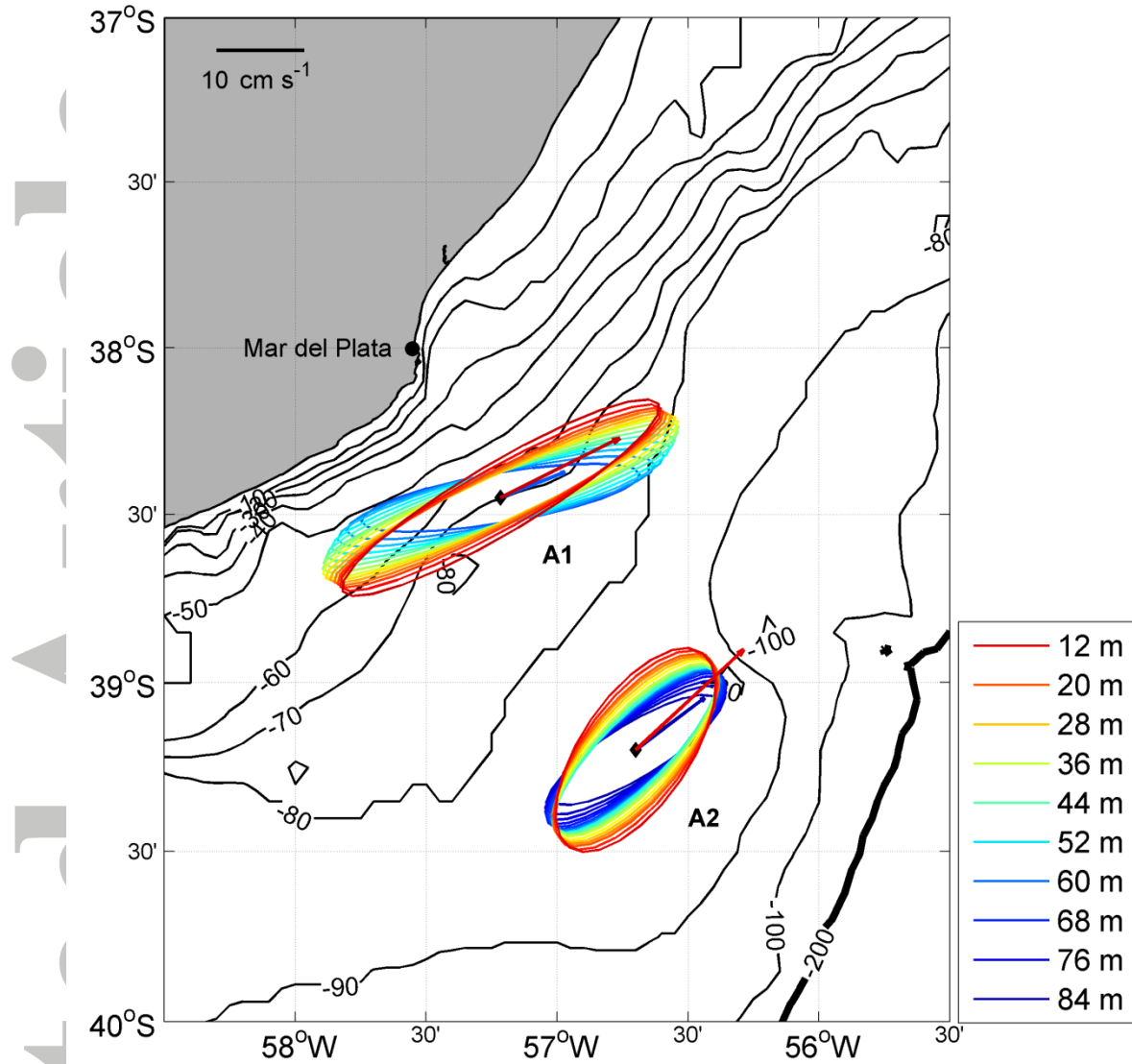
Figure 3: Bathymetry (m) (GEBCO, corrected by measurements from SHN) in the mooring area, A1 and A2 sites are indicated by the black diamonds. Thin black lines represent isobaths every 10 m from 10 to 100 m depth. The 200 m isobath is indicated by the heavy black line. Also shown are the variance ellipses of in-situ currents at all sampled depth levels (reference scale at right). The record-length mean of the shallowest and deepest velocity at each site are indicated by arrows (reference scale on upper left corner).
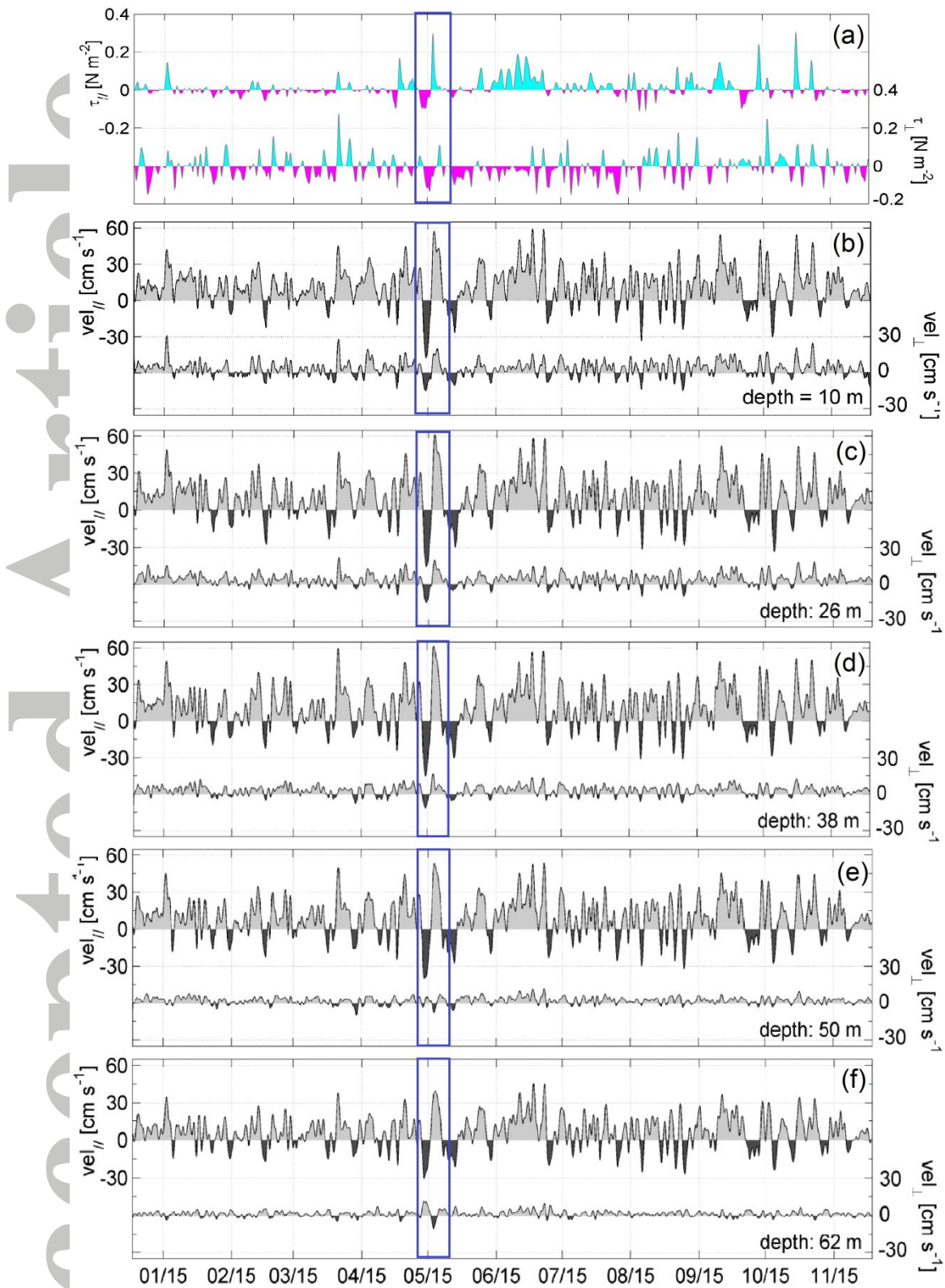
Figure 4: (a): Along (top) and cross-bathymetry (bottom) wind stress [N m^{-2}] at A1 from ERA-Interim. (b) to (f): Along and cross-bathymetry velocity [cm s^{-1}] at selected depths at A1. The blue rectangle indicates the timing of an extreme flow reversal event described in section 4.3. Along-bathymetry velocities are positive towards the ENE and cross-bathymetry velocities are positive towards the WNW (onshore).
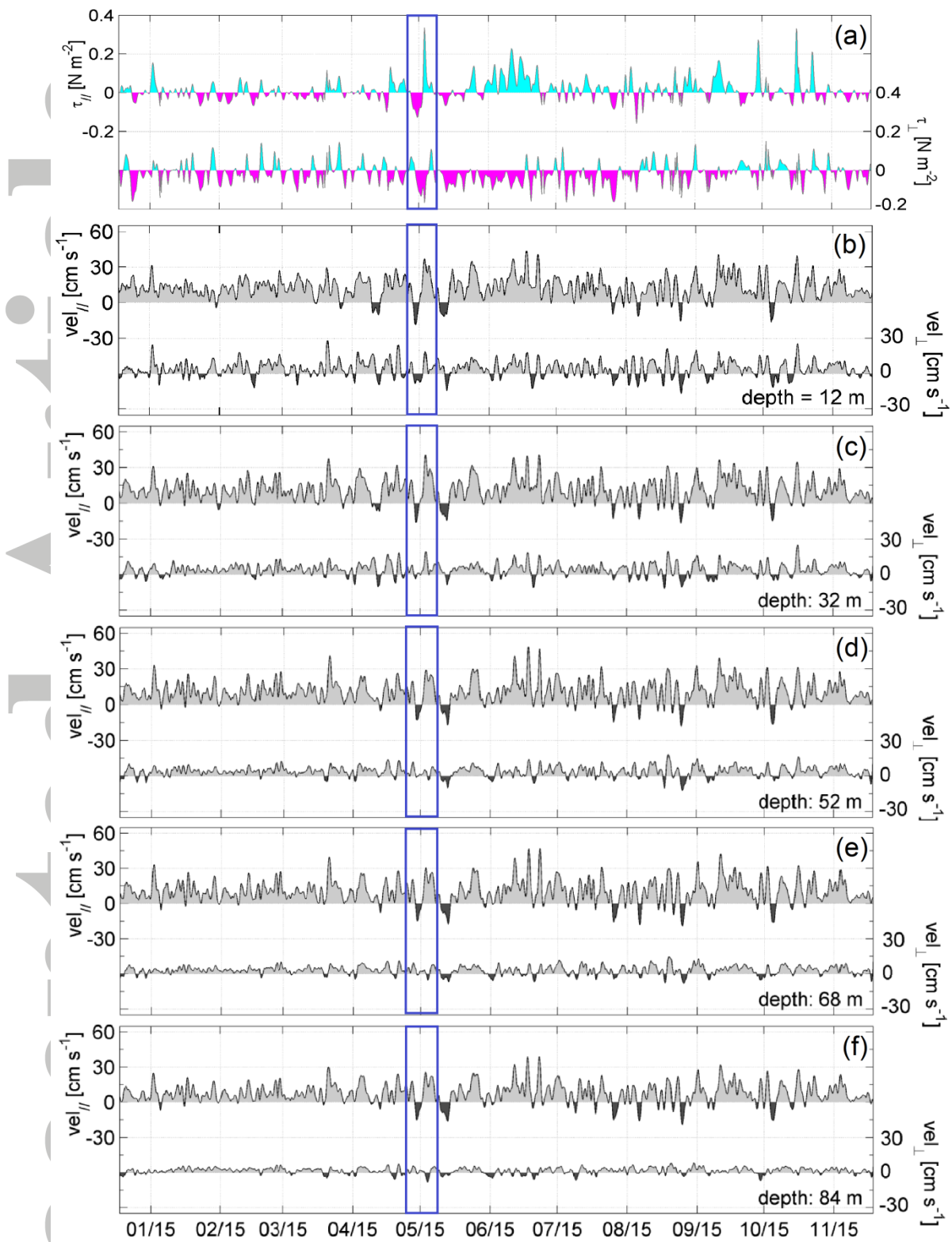
Figure 5: Same as Figure 4 at A2.
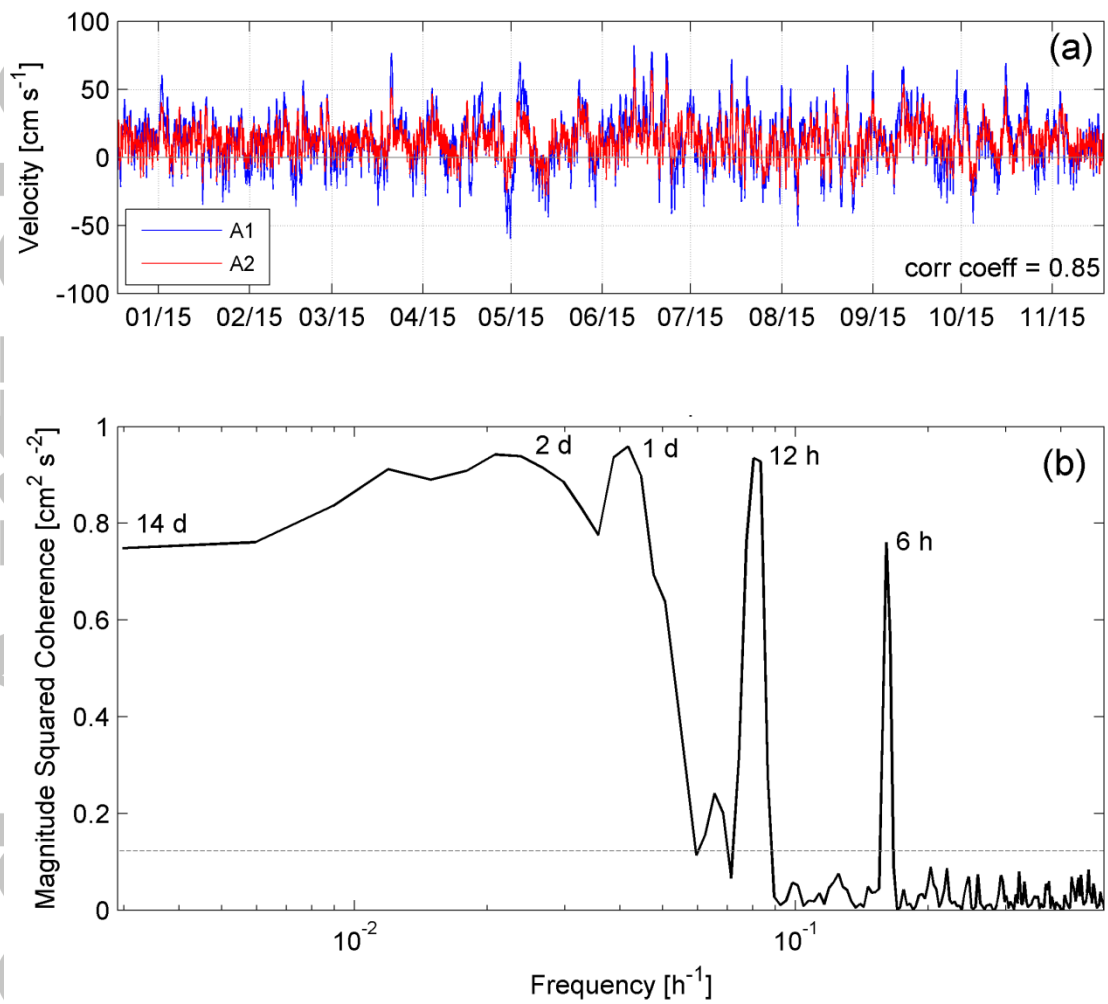
Figure 6: Non-filtered along-shore barotropic velocity time series at A1 (blue) and A2 (red) (a) and coherence spectrum (b). The horizontal dashed line in (b) repesents the 95% confidence level.
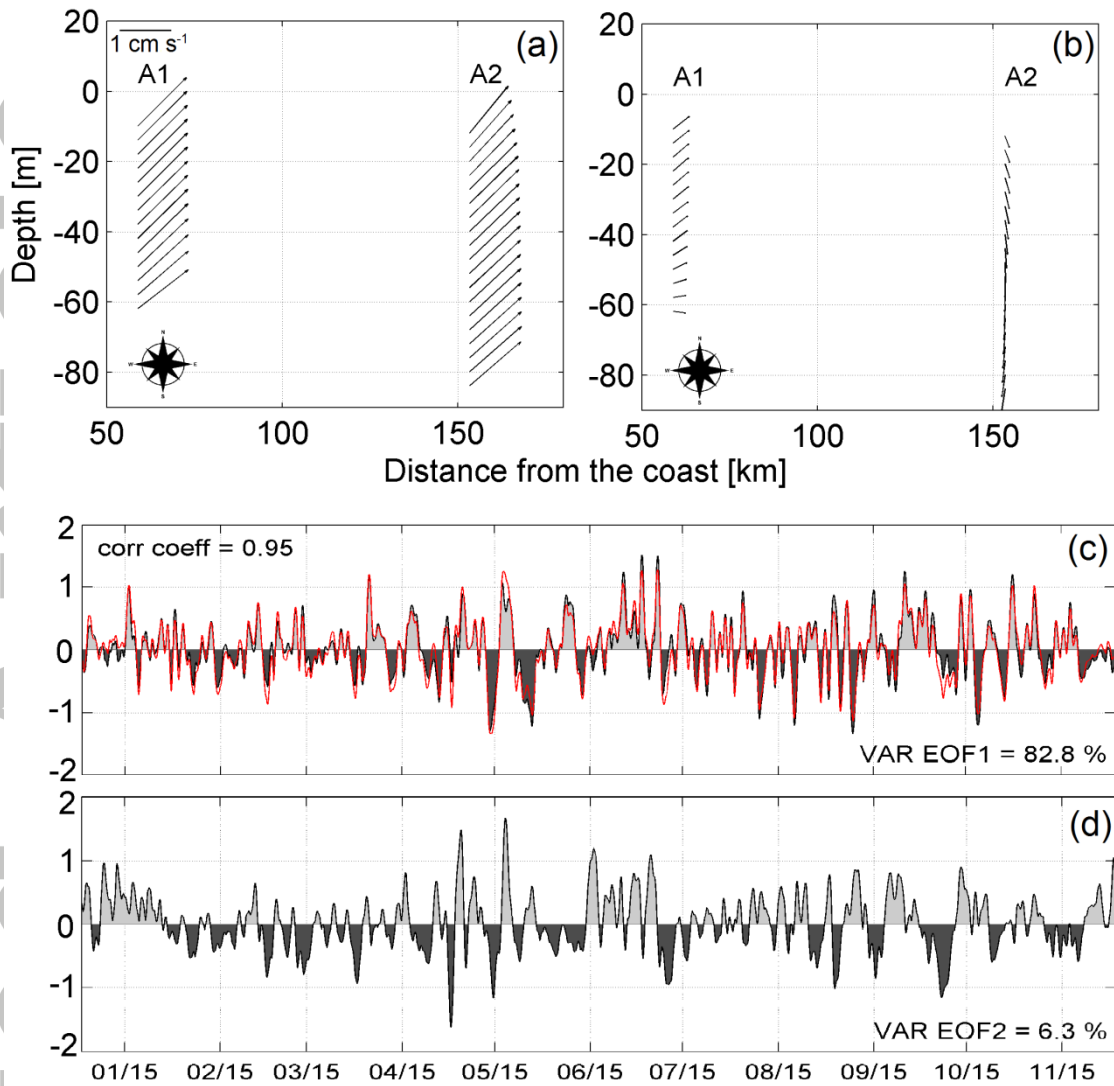
Figure 7: Spatial patterns and normalized time series of the 1st (a, c) and 2nd EOF mode (b, d) of the barotropic velocity component at A1 and A2. The red line in (c) shows the normalized along-shore barotropic velocity at A1. Vectors shown in (a) and (b) represent the geographical direction in the horizontal plane (zonal and meridional), the axis indicates the location associated with each vector (to what deployment and what depth level each horizontal vector corresponds).
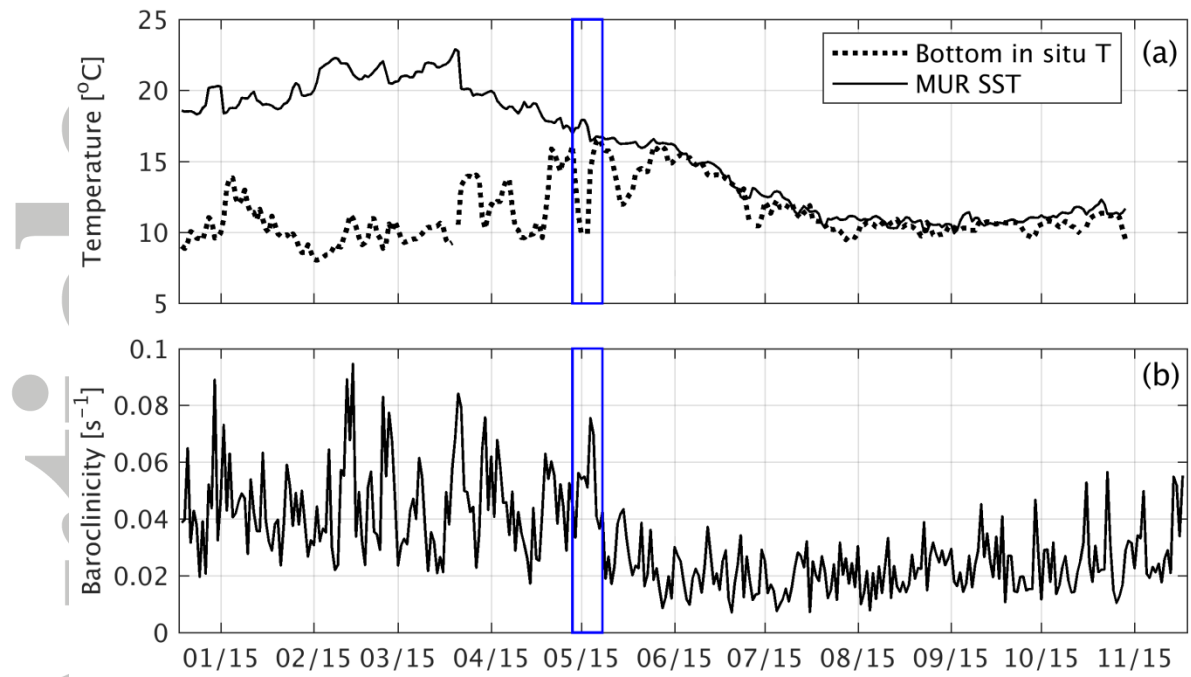
Figure 8: (a) Satellite SST (thin line) and in-situ bottom T (dashed line) at A1. (b) Baroclinicity index from in-situ velocities. The blue rectangle indicates an extreme flow reversal event described in section 4.5.
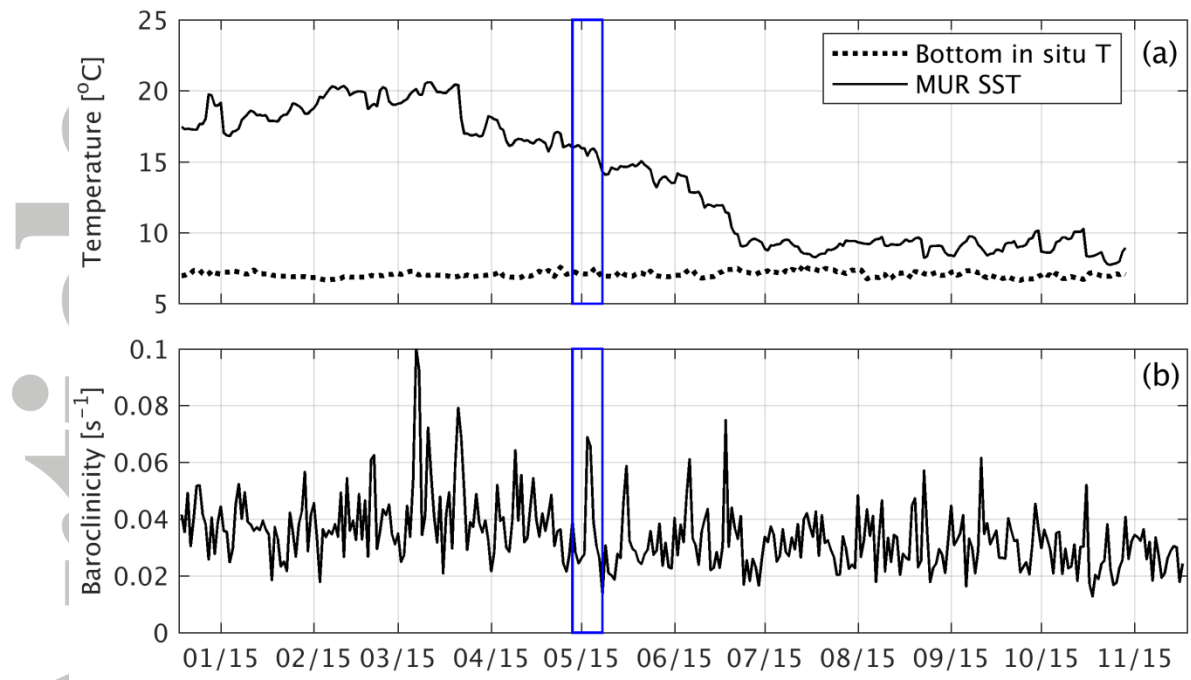
Figure 9: Same as Figure 8 at A2.
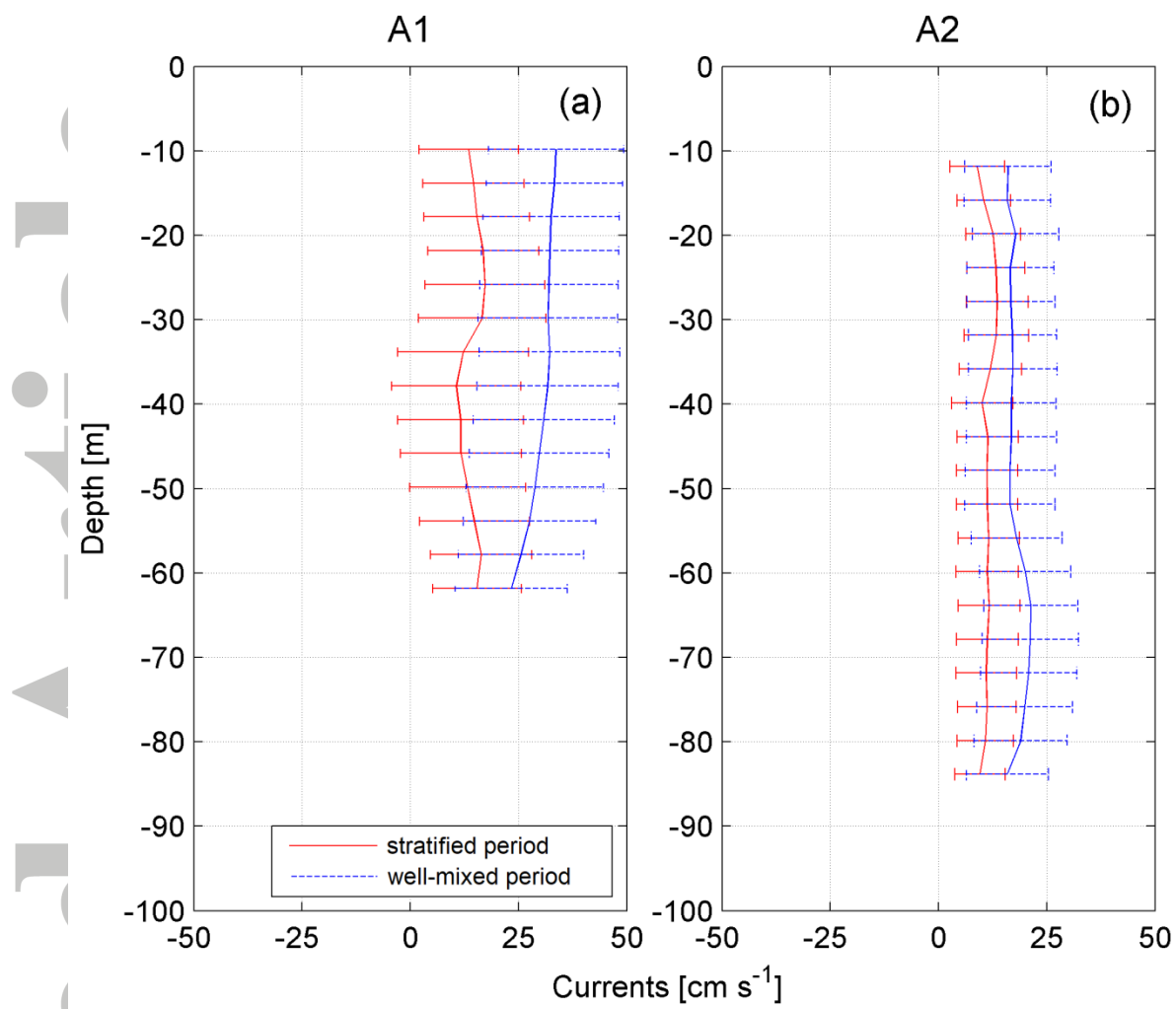
Figure 10: Time-averaged velocity and standard deviation of the along-shore currents for the stratified period (red) and the well-mixed period (blue) at A1 (a) and A2 (b).
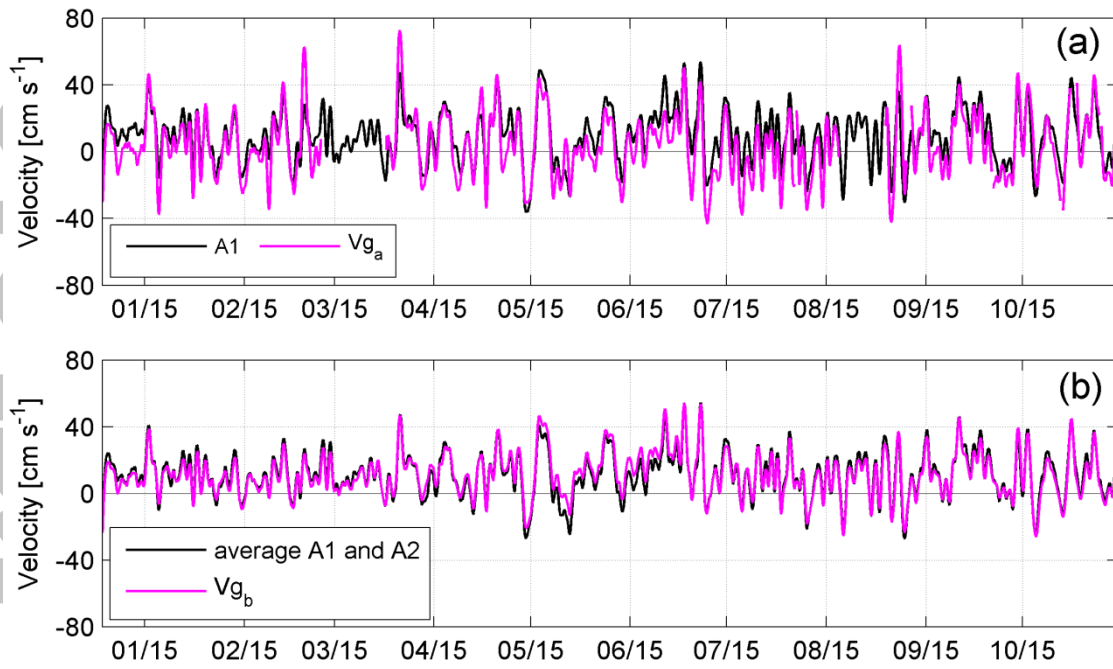
Figure 11: (a) Along-shore barotropic component of the velocity excluding the Ekman layer (black) averaged over A1 and A2 and absolute geostrophic velocity computed from SSH gradients between TG and A1 (magenta); (b) along-shore barotropic component at A1 excluding the Ekman layer (black) and absolute geostrophic velocity computed from SSH gradients between A1 and A2 (magenta).
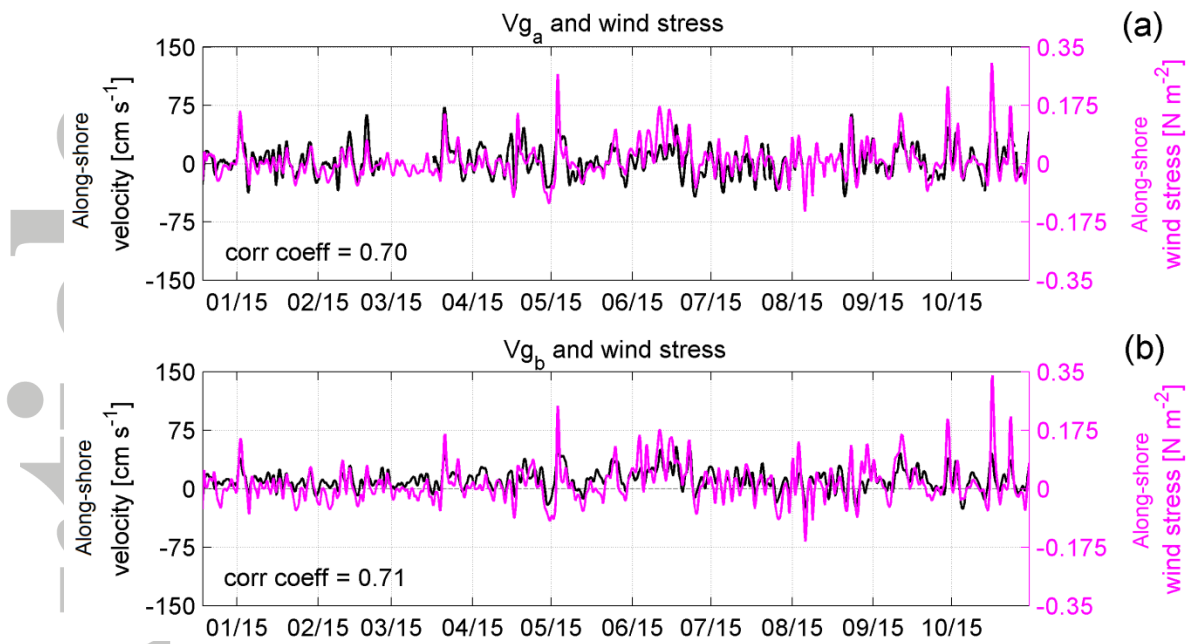
Figure 12: Along-shore absolute geostrophic velocity (black line) between TG and A1 (a) and between A1 and A2 (b), along-shore and wind stress from ERA-Interim (magenta line). See Figure 1 for reference.
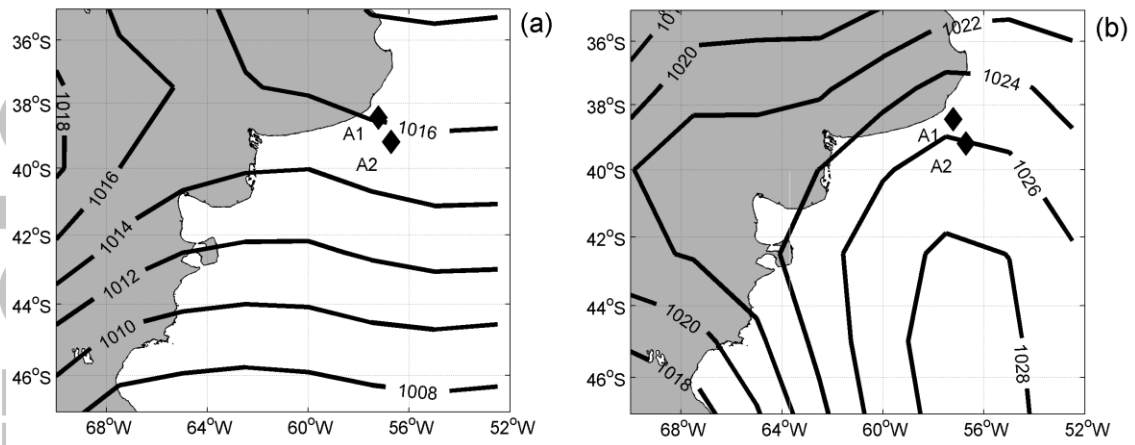
Figure 13: (a) Mean SLP in autumn (AMJ) 2015 and (b) SLP on 28 April 2015.

Table 1: Mean speed and direction (relative to the True North), and maximum velocity at all depths for both deployments.

Depth [m]	A1			Depth [m]	A2		
	Mean speed [cm s^{1}]	Mean direction [º]	Maximum velocity [cm s^{-1}]		Mean speed [cm s^{-1}]	Mean direction [º]	Maximum velocity [cm s^{-1}]
10	12.0	63.4	61.3	12	13.1	47.1	47.4
14	11.8	60.7	62.3	16	12.7	45.2	50.4
18	11.5	59.2	61.5	20	12.3	44.4	49.9
22	11.3	58.7	63.8	24	12.0	44.8	48.7
26	11.0	58.5	64.1	28	11.9	44.7	48.0
30	11.0	59.5	64.6	32	11.9	44.4	44.8
34	11.0	61.2	64.3	36	11.8	44.3	44.3
38	10.7	62.9	63.2	40	11.7	44.5	44.7
42	10.2	64.0	59.8	44	11.6	44.9	46.1
46	9.6	65.1	58.0	48	11.5	45.2	48.3
50	9.0	66.3	55.0	52	11.4	45.5	50.6
54	8.2	66.9	52.9	56	11.2	45.8	50.1
58	7.4	68.0	50.4	60	11.1	46.3	49.5
62	6.2	68.3	46.6	64	11.0	46.8	48.1
-	-	-	-	68	10.8	47.5	47.5
-	-	-	-	72	10.7	49.0	46.2
-	-	-	-	76	10.4	50.8	44.8
-	-	-	-	80	9.9	53.0	42.8
-	-	-	-	84	7.7	52.9	38.9

**Appendix**

Table A1: Comparison of wind data obtained at the oceanographic buoy located at 56.2^0W, 39.9^0S (Paniagua *et al*, 2018) between 22 December 2014 and 22 January 2015 and NCEP and ERA-Interim reanalyses, and the multi-platform CCMP data. Angle is the angle that results from the vector correlation estimate.
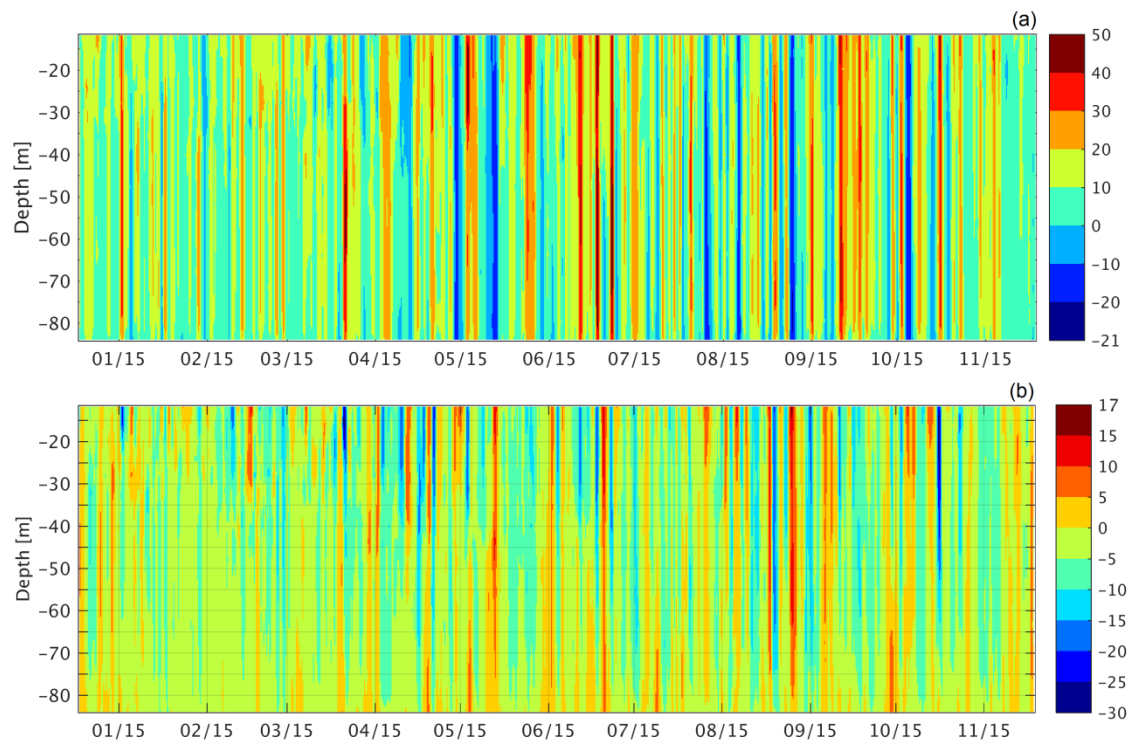
Buoy vs	Vector correlation coefficient	Angle [deg]	RMSD [m s^{-1}]
NCEP	0.93	12	3.7
ERA-Interim	0.96	18	1.1
CCMP	0.97	14	1.2
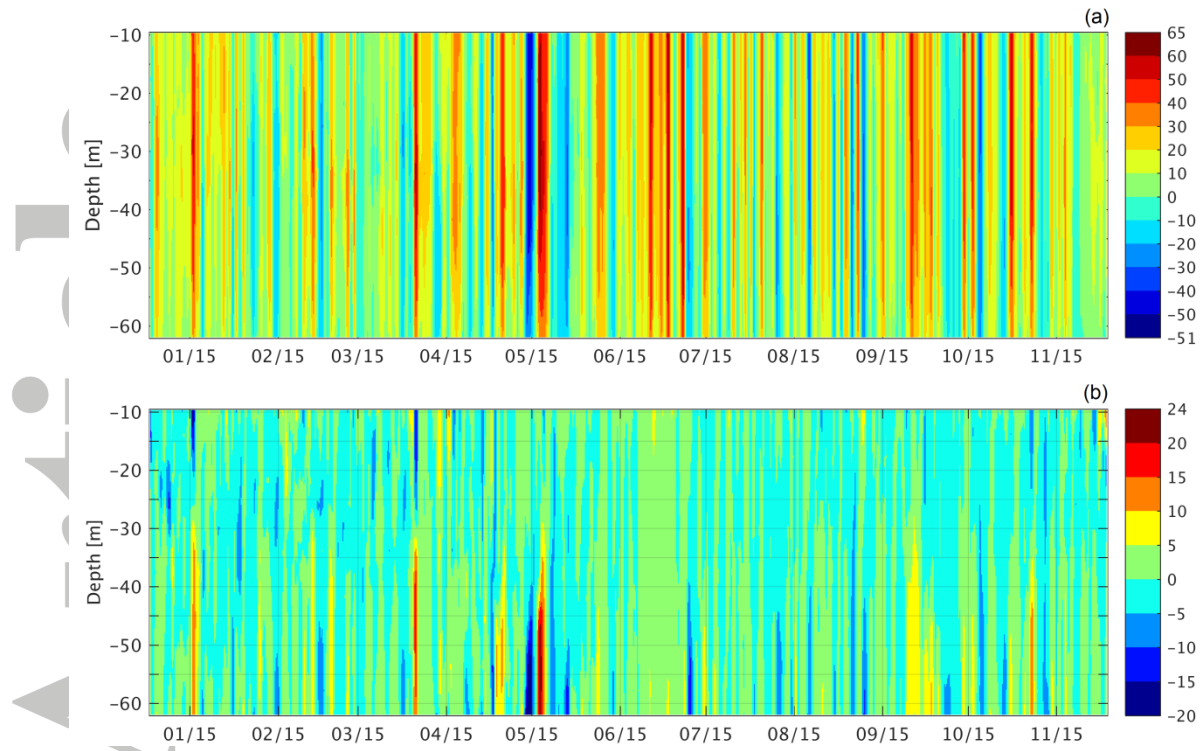
Figure A1: Hovmöller diagram of the 48 h low-pass filtered in-situ velocity [cm s^{-1}] at A1 for the along-shore component (a) and for the across-shore component (b).

Figure A2: Hovmöller diagram of the 48 h low-pass filtered in-situ velocity [cm s^{-1}] at A2 for the along-shore component (a) and for the across-shore component (b).
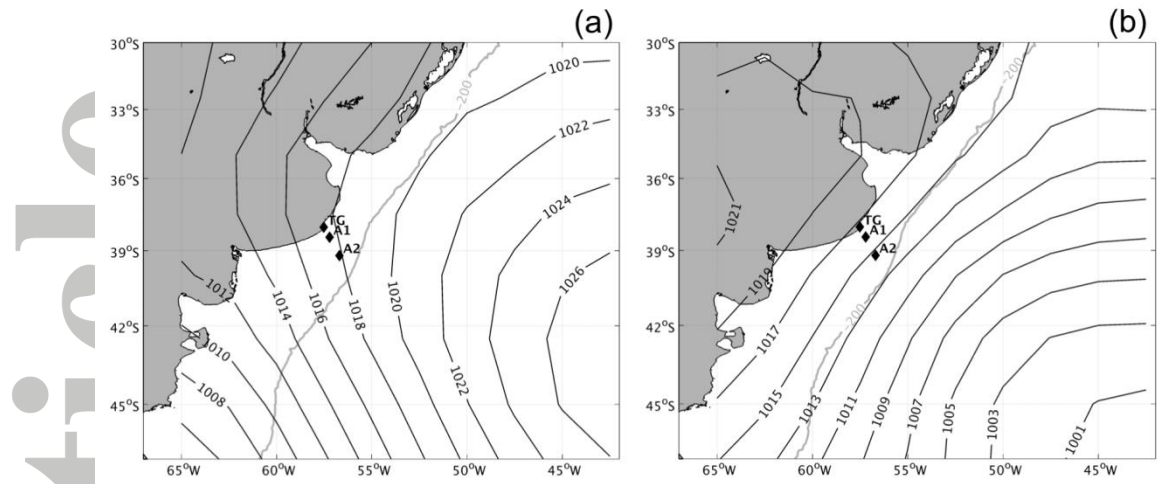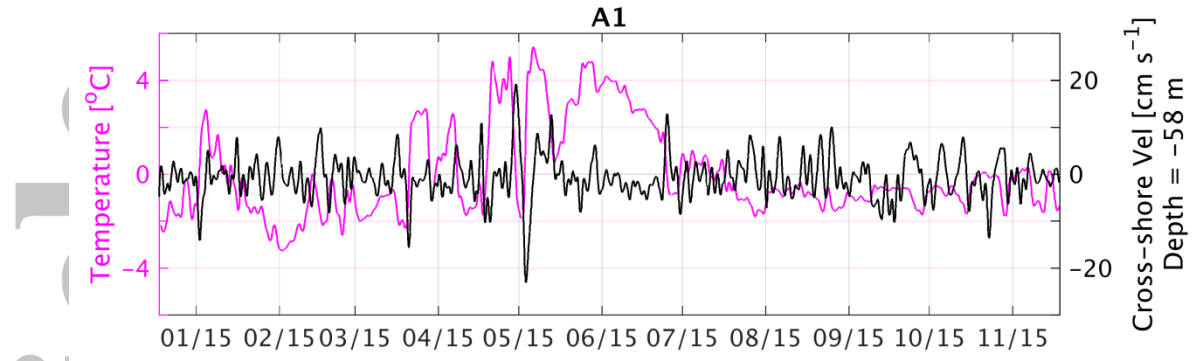
Figure A3: SLP [hPa] composite for the days of lowest (a) and highest (b) values of the first EOF mode of the barotropic velocity shown in Figure 7c (a).
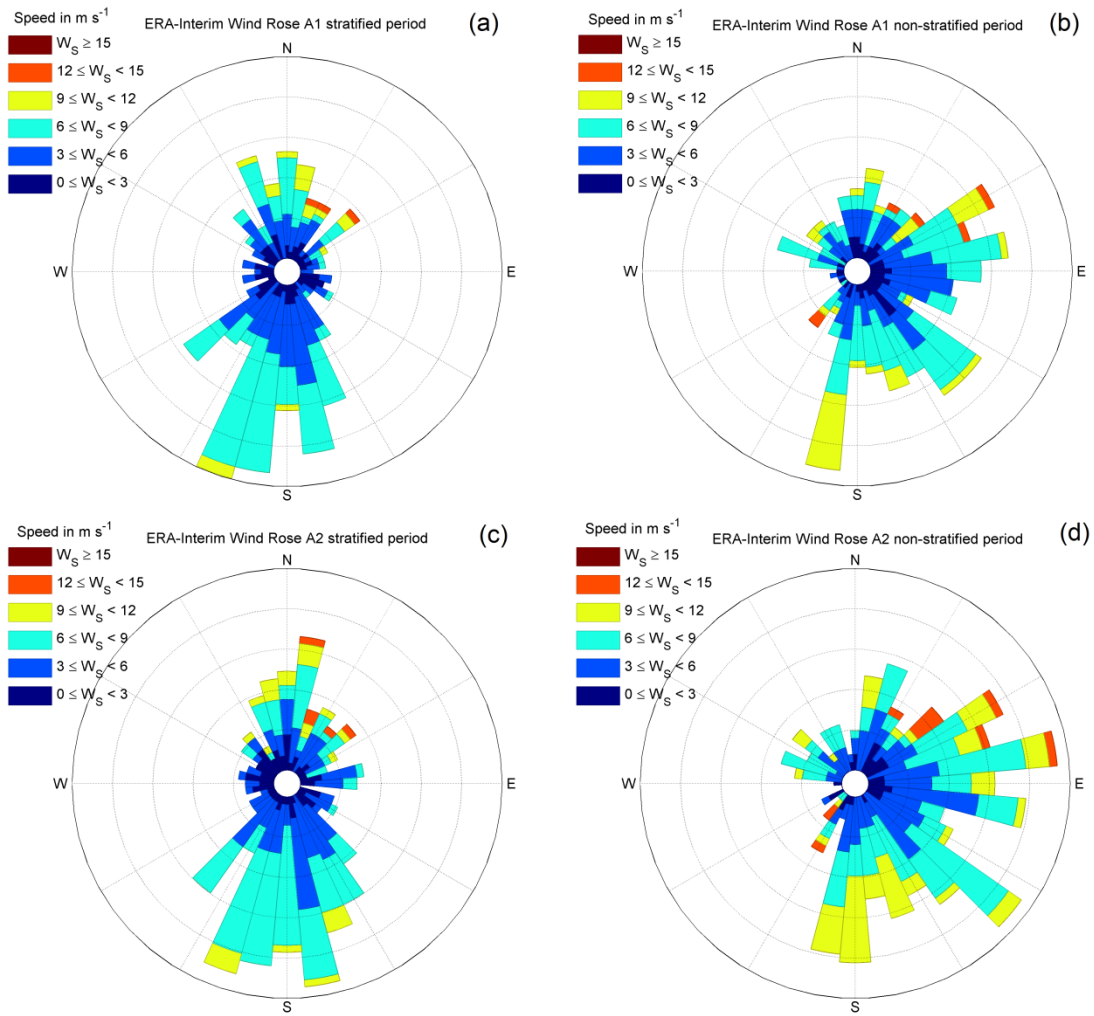
Figure A4: Bottom T at A1 (red) and cross-shore velocity in the second depth level closer to the bottom (58 m depth). Both time series were low-pass filtered with a cut-off period of 48 h.
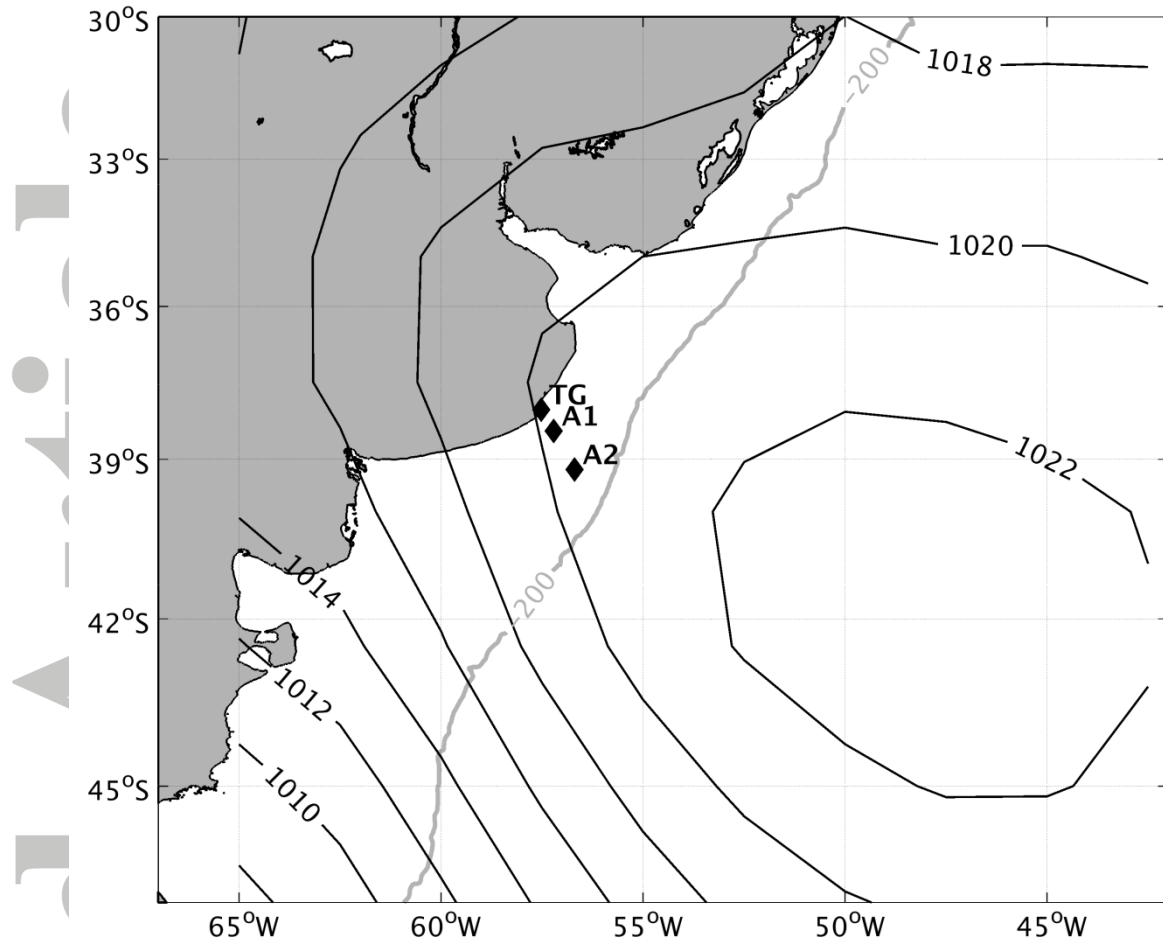
Figure A5: Wind rose of the ERA-Interim wind stress at A1 (a and b) and A2 (c and d) for the stratified period (a and c, 1 January 2015 to 31 March 2015) and the non-stratified period, (b and d, 1 July 2015 to 30 September 2015).
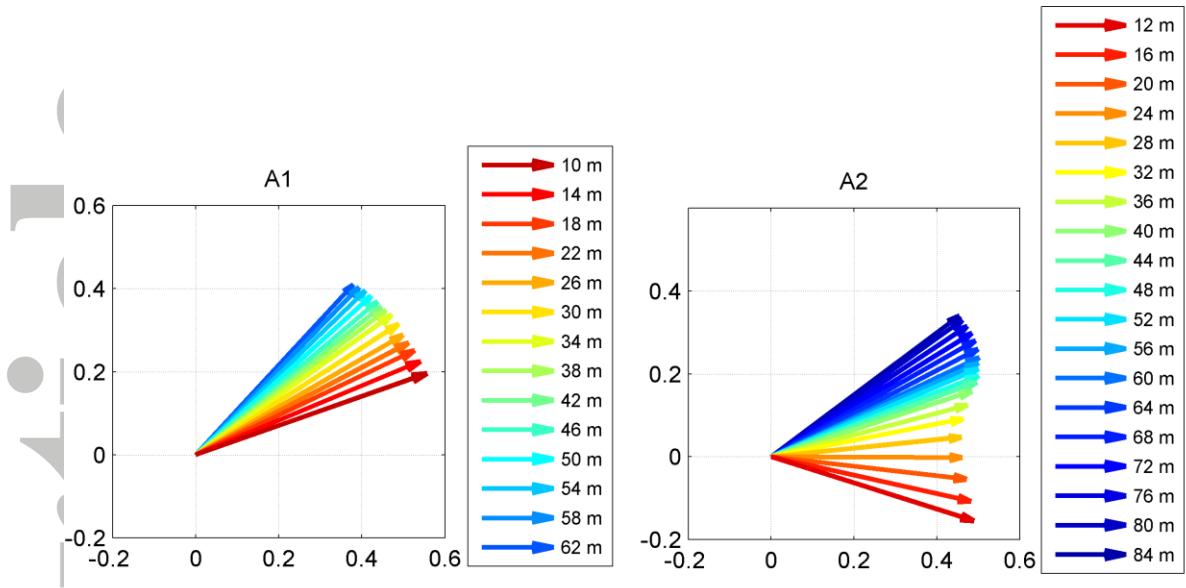
Figure A6: Vector correlation between ERA-Interim wind stress and in-situ velocity observations, at A1 (a) and A2 (b).

Figure A7: SLP [hPa] composite for the days of in-situ currents reversal of the across-section component at the shallowest level of A1.